OE Optical Engineering

RESEARCH PAPER

Simulation-assisted prediction of residual stress-induced failure during powder bed fusion of metals using a laser beam

Hannes Panzer,* Daniel Wolf, and Michael F. Zaeh
Technical University of Munich, Institute for Machine Tools and Industrial Management, TUM School of Engineering and Design, Garching, Germany

ABSTRACT. Conventional manufacturing technologies, such as milling or casting, often reach their limits when complex geometries are involved. Additive manufacturing (AM) is a reasonable alternative for the fabrication of such parts. In particular, the powder bed fusion of metals using a laser beam (PBF-LB/M) has already been established in industrial production because it allows for the manufacturing of parts with high mechanical properties and a fine resolution. However, due to an uneven heat input during the process, the parts being manufactured are prone to thermally driven stress-induced cracking. We introduced an approach to predict regions within PBF-LB/M-manufactured parts that exhibit a high susceptibility to stress-induced fracture by means of numerical simulation. Previously identified and calibrated failure models for Inconel 718 were integrated into a PBF-LB/M process simulation, which uses the finite element method. Based on an implemented damage indicator, for which the failure models served as an input, critical locations due to the successive build-up of mechanical stresses and strains during layer-wise manufacturing were identified. The determined regions were experimentally validated by comparing the experimental results to the simulative predictions. An AM-adapted calibration approach allowed for a reliable prediction of crack-prone regions within PBF-LB/M-manufactured parts. An experimental method underestimated the susceptibility to failure, whereas a combined experimental and simulative approach overestimated it. The obtained results of this study contribute to the concept of first-time-right manufacturing as critical regions can be modified before the actual manufacturing process. The presented approach is also anticipated to be applicable to predicting crack formation between a solid part and its support structure.

Keywords: additive manufacturing; powder bed fusion of metals using a laser beam process simulation; stress-induced fracture; failure modeling; crack formation and propagation

Paper 20240207SS received Mar. 2, 2024; revised Jun. 27, 2024; accepted Aug. 29, 2024; published Oct. 4, 2024.

1 Introduction

Compared to conventional manufacturing technologies such as milling or casting, additive manufacturing (AM) processes are far less restricted in manufacturability of geometrically complex-shaped parts.[1] Therefore, various industrial sectors use this technology, for example, the aerospace and medical technology sectors.[2] Especially, the powder bed fusion of metals using a laser beam (PBF-LB/M), a process in which thin layers of metallic powder are repeatedly applied and

*Address all correspondence to Hannes Panzer, hannes.panzer@iwb.tum.de

melted by a laser beam, has proven to be capable of producing parts with excellent mechanical properties.[3] However, residual stresses evolve during the part manufacturing due to an inhomogeneous heat input.[4] These stresses can lead to a reduction of the service life of parts[5] and can even accumulate to such an extent that residual stress-induced cracking can occur during the building process.[6] Being able to predict critical regions and evaluating the cracking susceptibility is of high importance to allow for a part redesign or local process parameter adaptions to mitigate a crack initiation or propagation.[7] A failure prediction can also contribute to detecting and avoiding potential build job failures prior to the actual printing process.

Lyu et al.[8] applied three simulation steps for the numerical representation of the PBF-LB/M process and the failure behavior of parts manufactured of AlSi10Mg. First, a thermo-mechanical finite element (FE) process simulation on a small scale was executed, considering PBF-LB/M-specific process parameters, such as the scan pattern. In a second step, the extracted inherent strains were transferred to a part-scale simulation, by which the distortion and the residual stresses in industrially relevant parts could be determined. Finally, the failure behavior of these objects was quantified by applying a particle method. By this, fractures occurring during the service life of additively manufactured parts could be predicted. However, the proposed approach does not allow for a prediction of a crack formation during the manufacturing process due to residual stresses.

Zhang and Zhang[9] estimated the crack occurrence between the support structure and the solid material by performing a weakly coupled thermo-mechanical FE simulation of the PBF-LB/M process. In their simulation, the authors considered the laser beam scan paths on stainless steel to determine the deformations and residual stresses during the manufacturing process. The maximum von Mises stress was utilized as an estimation for a potential crack formation. As no failure criterion was established, a quantitative prediction of fractures could not be obtained. The simulation approach is only applicable to estimations of crack formations between solid and support materials. The high computational costs of this estimate made it necessary to scale the simulation model down.

Another FE approach with a local heat source for the prediction of cracking at the solid-support interface was presented by Tran et al.[10] They set up and performed a novel calibration method for Inconel 718 (IN718) to determine a critical J-integral value, a non-linear elastic-plastic fracture parameter, as a threshold, at which residual stress-induced cracking was expected. They validated their implementations on further geometries for one set of process parameters. Their approach, however, does not consider a fracturing in regions of the solid part. Potential crack locations need to be known beforehand to adapt the FE mesh accordingly. Information about the crack propagation could not be given. The computational costs were rated as high, which was due to the explicit modeling of the fine support structures. This restricted the application area of this approach to small parts.

To circumvent the latter drawback, Tran et al.[11] worked out a global-local analysis approach. First, critical locations based on the resulting inherent strains were determined on a part scale. In the second step, the obtained locations were further evaluated by applying a J-integral analysis on a smaller scale. Modeling of the support structures by a homogeneous continuum further allowed for a reduction of the computational effort.

The global-local technique was applied and enhanced by Tran and To,[12] considering the contact area between the solid material and a teeth support structure. A relationship between the contact area and the critical J-integral could be obtained, allowing for an optimization of the support design in terms of the crack susceptibility on the one hand and support removal on the other hand. The results presented by the authors are, however, restricted to horizontal contact surfaces.

Bresson et al.[13] evaluated commercial FE software tools (Autodesk Netfabb, Oqton Amphyon, Altair Inspire, and ESI Additive Manufacturing) in terms of their predictive capabilities of crack formation at the solid-support interface in 316L stainless steel and, therefore, increased part deflections. None of the analyzed tools was able to predict fracturing in the mentioned region. Therefore, the authors utilized an Abaqus subroutine for the consideration of a ductile damage initiation criterion, in which the damage was assumed to change linearly with the deformation. The simulation results only showed a partial correspondence with experimental validations. A failure within the bulk material was not considered. Non-linearities of the fracture

behavior were not taken into account. The fracture model constants had no physical basis and were dependent on the element size of the FE mesh.

Based on this overview, it can be concluded that no approach exists in the literature capable of predicting and quantifying the fracture formation in the solid region of parts manufactured by PBF-LB/M. Recent studies were focused on the modeling of crack prediction in the solid-support interface. The approaches are either restricted in an actual prediction of crack locations or lack a physical basis and comprehensive model calibration. The computational effort for the conduction of the simulations was often characterized as high. Research results with regard to this topic are scarce for the material IN718.

Therefore, this work focused on the evaluation of recently calibrated ductile failure criteria[14] based on the modeling approaches from Rice-Tracey (RT)[15] and Johnson-Cook (JC)[16] in their capabilities of appropriately predicting residual stress-induced fractures.

The following research questions were addressed over the course of this study:

- How much is the approach of a physically based calibrated cumulative damage indication an effective and efficient means to model a stress-induced fracture formation?
- Which failure models and calibration approaches allow for a reliable prediction of regions with a high susceptibility of residual stress-induced failure in the solid part for IN718?
- To what extent are the implemented failure models capable of predicting the crack length as well as the crack path and the propagation direction?

2 Materials and Methods

In this section, the theoretical basics to predict cracking along with a description of the operating principle to localize the fracture locations are introduced. The integration of the calibrated model parameters into the *iwb* simulation tool *AscentAM*, which was introduced by Bayerlein,[17] and the underlying FE tool *CalculiX*[18] are described below. The preparatory work for the model validation is explained afterward.

2.1 Underlying Formulas

The ductile failure models based on RT and JC were utilized in this study to evaluate their respective fracture prediction capabilities. The failure models, along with a means for indicating damage, are described below.

2.1.1 *Equivalent plastic failure strain*

The RT and the JC models, describing crack initiation and propagation phenomena in ductile materials, account for the stress triaxiality σ^* according to

$$\sigma^* = \frac{\sigma_\mathrm{m}}{\sigma_\mathrm{eq}}, \tag{1}$$

with the mean or hydrostatic stress σ_m and the von Mises equivalent stress σ_eq. In the RT model, the critical strain at a uniaxial stress state is related to that of a triaxial state by the following equation of the equivalent plastic failure strain $\varepsilon^\mathrm{f}_\mathrm{eq,RT}$:

$$\varepsilon^\mathrm{f}_\mathrm{eq,RT} = 1.65 \cdot \varepsilon_0^\mathrm{RT} \cdot \exp\left(-\frac{3}{2} \cdot \sigma^*\right), \tag{2}$$

where $\varepsilon_0^\mathrm{RT}$ represents the model-specific calibration constant. The JC model is an alternative empirical approach defined by

$$\varepsilon^\mathrm{f}_\mathrm{eq,JC} = (d_1 + d_2 \cdot \exp(d_3 \cdot \sigma^*)) \cdot (1 + d_4 \cdot \ln(\dot{\varepsilon}^*)) \cdot (1 + d_5 \cdot T^*). \tag{3}$$

In contrast to the RT model, the JC model is comprised of more calibration constants concerning the stress triaxiality ($d_1 - d_3$) and additionally allows for calibration of the strain rate (d_4) and the temperature (d_5). The parameter T^* in Eq. (3) is the dimensionless temperature and is defined as

$$T^* = \frac{T - T_{\mathrm{ref}}}{T_{\mathrm{M}} - T_{\mathrm{ref}}}. \tag{4}$$

Here, T represents the applied temperature, T_{ref} the reference temperature, and T_{M} the melting temperature of the utilized material. The dimensionless strain rate $\dot{\varepsilon}^*$ in Eq. (3) is written as

$$\dot{\varepsilon}^* = \frac{\dot{\varepsilon}^{\mathrm{p}}_{\mathrm{eq}}}{\dot{\varepsilon}_0}, \tag{5}$$

where $\dot{\varepsilon}^{\mathrm{p}}_{\mathrm{eq}}$ is the equivalent plastic strain rate and $\dot{\varepsilon}_0$ is the reference strain rate.

Each of the two presented models was calibrated by an experimental, an experimental and simulative, and an AM-adapted approach, as conducted by Panzer et al.[14] The calibration constants are shown in Table 2.

2.1.2 *Damage indication*

The equivalent plastic failure strains of Eqs. (2) and (3), respectively, serve as an input for a damage indicator, as proposed by Fischer et al.[20] To take into account the damage accumulation, which takes place during the plastic deformation of a body, the increment of the damage indicator is defined as

$$\mathrm{d}D = \frac{\mathrm{d}\varepsilon^{\mathrm{p}}_{\mathrm{eq}}}{\varepsilon^{\mathrm{f}}_{\mathrm{eq}}}. \tag{6}$$

Considering numerical tools such as the FE method, the damage indicator is calculated as follows:

$$D = \sum \frac{\Delta\varepsilon^{\mathrm{p}}_{\mathrm{eq}}}{\varepsilon^{\mathrm{f}}_{\mathrm{eq}}}, \tag{7}$$

with $\Delta\varepsilon^{\mathrm{p}}_{\mathrm{eq}}$ representing the equivalent plastic strain increment in each numerical increment or step. According to Fischer et al.[20] and Gao and Krishnamurthy,[21] this type of damage indicator is the simplest rule of a damage accumulation function, describing a linear relation between the damage and the equivalent plastic strain $\varepsilon^{\mathrm{p}}_{\mathrm{eq}}$.

Utilizing a damage indicator is expected to allow for a consideration of the accumulation of stresses and strains due to the layer-wise build-up of a PBF-LB/M part, eventually leading to the formation of residual stress-induced cracks. The onset of such a fracture is usually obtained when $D = D_{\mathrm{c}} = 1$,[20] with D_{c} being a critical value in terms of the cracking susceptibility.

2.2 Operating Principle of the Fracture Localization

In Fig. 1, the operating principle of the crack prediction code structure is illustrated. The process of the damage accumulation calculation is visualized by continuous lines. The thermo-mechanical simulation *AscentAM* provides the results for the stresses, which in turn are needed to calculate σ_{eq} and σ_{m}, resulting in σ^*. Along with the calibration constants (see Table 2), $\varepsilon^{\mathrm{f}}_{\mathrm{eq}}$ and afterward D are computed in each computational step. As long as the damage indicator is smaller than D_{c}, the next step, if existent, is started without deactivating elements. Within this loop, only the fracture results are generated, not changing the simulation results with regard to the displacements, strains, or stresses. Staying in this loop, the damage indicator increases with every computational step according to Eq. (7).

The extension of the code for the element deactivation, which allows for a representation of a crack propagation, is drawn by dashed lines. As soon as the damage indicator reaches or exceeds a user-specified critical value D_{c} in an integration point of corresponding elements, these elements are deactivated and are not considered further in the calculation process. The element deactivation process is dependent on the damage indicator in the integration points and not in the nodes, as the integration points are uniquely assigned to one element, which is, in general, not the case for nodes. The strains and stresses also have the highest precision in the integration points. The process is terminated as soon as no further step exists.

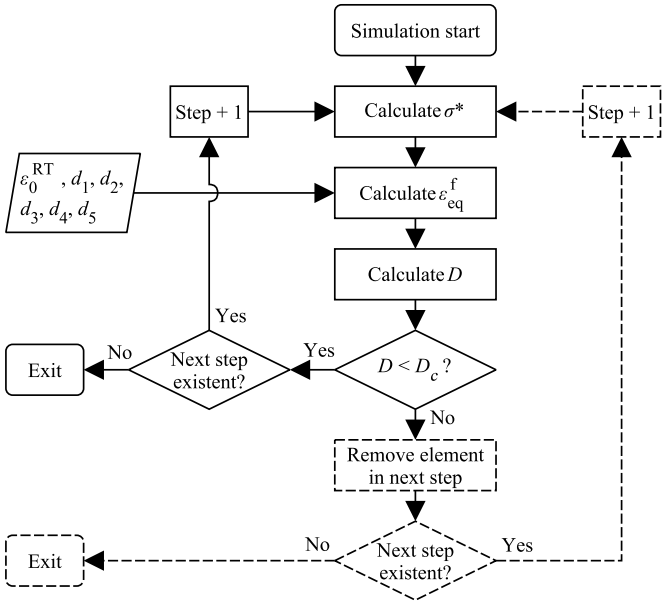

Fig. 1 Operating principle of the implemented code structure for the detection of failure within each finite element; the continuous lines illustrate the damage accumulation procedure, and the dashed lines outline the element deactivation.

2.3 Integration of the Calibrated Model Parameters

In the following, a description is given of how the fitting functions for the triaxiality and the temperature of the calibrated models are taken into account in the code implementations. The influence of the strain rate, considered by the parameter d_4 in Eq. (3), was not further considered over the course of this study. This can be explained by the fact that the effect on the failure strain ε_{eq}^f can be assumed to be negligible due to the small value of the parameter, as shown in Table 2. Also, a reliable value of the present strain rate during the manufacturing process could not be extracted.

2.3.1 *Triaxiality*

The calibrated models are only valid in the region of positive triaxiality because no calibration tests were performed, which would include data points in the negative half plane of this parameter space. Also, it is assumed that the crack formation during the building process is not attributed to compressive stress states.[16] Therefore, the calibrated models have to be modified for negative and low positive triaxialities.

Figure 2 schematically illustrates the extended curve for the failure models. The calibrated curve, shown by the continuous line, is always considered during the simulation as long as the

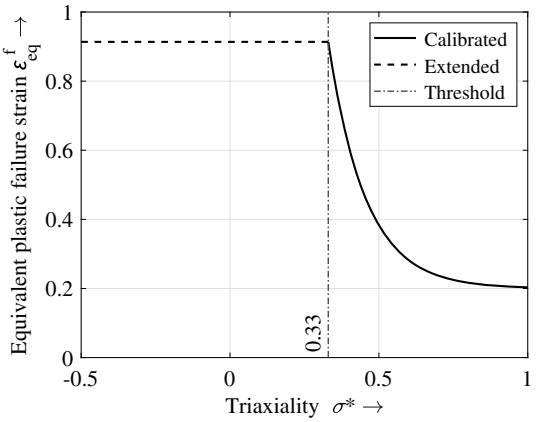

Fig. 2 Schematic illustration of the inclusion of the triaxiality behavior.

triaxiality holds a value greater than or equal to 0.33 in the corresponding integration point. This threshold was chosen as the calibration values shown in Table 2 did not fall below this value and the validity of the corresponding equivalent plastic strains cannot be guaranteed. If the triaxiality reaches a value smaller than this threshold (marked by the dot-dashed line), the equivalent plastic failure strain ε_{eq}^{f} at this threshold value is used, which is illustrated by the horizontal dashed line.

2.3.2 *Temperature*

The following statements only apply to the experimentally calibrated JC model because only there the temperature is considered.

As shown by Panzer et al.,[14] the temperature calibration was only conducted up to 250°C, comprising the steady state temperature of 200°C during the processing of IN718 via PBF-LB/M.[17] As proposed by Johnson and Cook,[16] the equivalent plastic failure strain ε_{eq}^{f} is linearly related to the temperature. At higher temperatures, this relationship cannot be assumed anymore without experimental tests. This is why in the implementation for the temperature dependence, the strain is kept at a constant value if the current temperature is above the steady state temperature. This idea is schematically illustrated in Fig. 3, where the continuous line shows the area of the calibrated results and the dashed line illustrates the temperature domain, in which the equivalent plastic failure strain ε_{eq}^{f} is kept constant.

To consider the temperature impact on the code structure, the reference temperature and the melting temperature of the utilized material, as stated in Eq. (4), had to be specified. For this, T_M was set to 1326.85°C,[22] whereas T_{ref} was chosen to be 24.3°C as this was the test temperature of the reference geometries for the purely experimental calibration.[14]

2.3.3 *Additional modifications*

The thermo-mechanical process simulation AscentAM includes two computational steps per layer compound, which are characterized by non-physical material changes from purely elastic to completely plastic, and from purely plastic to the actual IN718 material parameters. These were introduced to allow for the representation of the PBF-LB/M-characteristic self-healing effect. However, within this study, these computational steps were excluded as the resulting strains would have falsified the fracture results and did not account for an actual accumulation of failure.

During the fracture simulations, only positive strain differences $\Delta\varepsilon_{eq}^{p}$ are considered. Through this, compressive strains do not contribute to the damage accumulation process.

2.4 Validation Preparations

To validate the simulation implementations, appropriate geometries were to be selected, which will be described below. Information about the measurement of the built specimens will be given afterward.

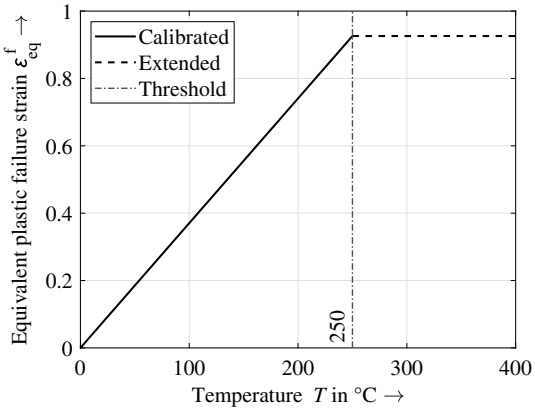

Fig. 3 Schematic illustration of the consideration of the temperature behavior.

2.4.1 *Geometries*

The general dimensions of the validation geometries are visualized in Fig. 4, in which z denotes the building direction. The wall thickness parameter a was chosen to be 0.5 mm (specimen A) and 0.3 mm (specimen B), respectively, resulting in two validation geometries. The two wall thicknesses were chosen to allow for the formation of cracks with varying lengths in the critical area, at which stresses and strains were expected to accumulate. By this, the predictive capabilities of the proposed modeling approach for both the crack initiation ($a = 0.5$ mm) and the crack formation and propagation ($a = 0.3$ mm) were validated.

2.4.2 *Convergence study*

The geometries were created by computer-aided design (Inventor Professional 2023, Autodesk GmbH, Germany) and, subsequently, were meshed (HyperMesh 2019, Altair Engineering GmbH, Germany). In that respect, the geometries were segmented to allow for a local mesh refinement in the critical region of the respective crack samples. The refined FE mesh of linear tetrahedrons was applied 0.3 mm above and below the critical area for both geometries, respectively. For specimen A, the boundary for the finer mesh in the x-direction was set to 0.6 mm behind the critical region. For specimen B, this value was set to 6 mm because an increased crack length was expected. The element sizes were varied within the mentioned boundaries and were set to 0.1, 0.05, 0.03, and 0.025 mm. Outside this region, the element size was gradually increased to 0.5 mm within the remaining part. The simulation of the layer-by-layer manufacturing was conducted by a layer-wise activation of elements with a layer compound height of 1 mm and a flash exposure strategy. The element size in the build plate was chosen to be 10 mm. For each geometry-element set, the maximum plastic equivalent strain was evaluated.

As visualized exemplarily for specimen A in Fig. 5, which also shows the number of elements in the mesh refinement region, a converging behavior was achieved after an element size of 0.03 mm was utilized. This element size was, therefore, used for the remaining simulations concerning the validation.

2.4.3 *Manufacturing process*

Specimen A and specimen B were printed five times each on a PBF-LB/M machine (M400-1, EOS GmbH, Germany), using IN718 (MetcoAdd 718C, OC Oerlikon Management AG, Switzerland) as the powder feedstock material. The used process parameters for the manufacturing of the presented specimens are shown in Table 1. The samples were printed on a 5 mm tall base to avoid an unintentional modification of the formed cracks due to a release of residual stresses or an interaction of the cut-off device and the part wall. The specimens were cut off by electrical discharge machining (MV2400S, Mitsubishi Electric, Japan).

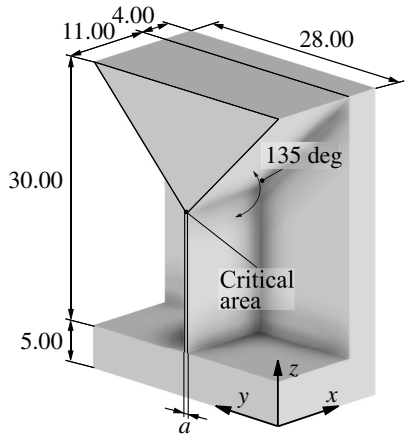

Fig. 4 Dimensions of the crack sample geometries in mm; z denotes the building direction.

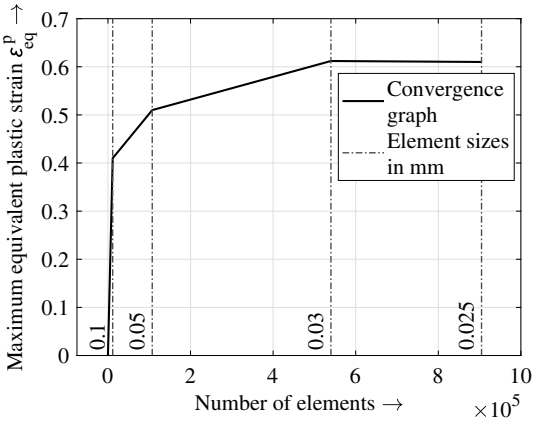

Fig. 5 Result of the conducted convergence study for specimen A; the number of elements refers to the mesh-refined region in the critical area.

Table 1 Process parameter set for the manufacturing of the specimens.

Parameter	Laser power	Scan speed	Hatch distance	Layer height
Value	285 W	960 mm/s	0.11 mm	0.04 mm

2.4.4 *Crack measurement*

The locations (global analysis) as well as the length, path, and appearance (local analysis) of the cracks within the samples were analyzed in the x-z-plane from both sides using a digital microscope (VHX 7000, Keyence Corp., Osaka, Japan) with coaxial lighting. As, within each specimen, the crack lengths on each side differed, a mean crack length per sample was calculated. Further information about the measurement approach can be found in Panzer et al.[7] Also, the critical region was analyzed in the y–z-plane, to further investigate the crack appearance. The obtained measurement results were used for the validation of the simulative findings.

3 Results and Discussion

3.1 Verification

To verify the implementations of this study, the conformity with already present implementations was analyzed. Afterward, the functionality of the damage accumulation was tested. These verification processes are described in the following.

3.1.1 *Matching of present implementations*

The already present calculation of the von Mises stress in *CalculiX* was replicated in the created subroutines to verify the functioning of the implementations. Various simulation results have shown a full consistency between the standard results and those from the extended version. Through this, proper exchange of parameters and transfer of data within the extended tool structure was ensured.

3.1.2 *Damage accumulation*

In Fig. 6(a), the continuous increase of the mean damage indicator of crack-prone elements in the critical region with an increasing build time is visualized. The values within the integration points were extracted after each computational step as soon as the part height had reached the critical area during the build-up process. The resulting graph can be divided into three distinct zones, which are also highlighted in Fig. 6(b).

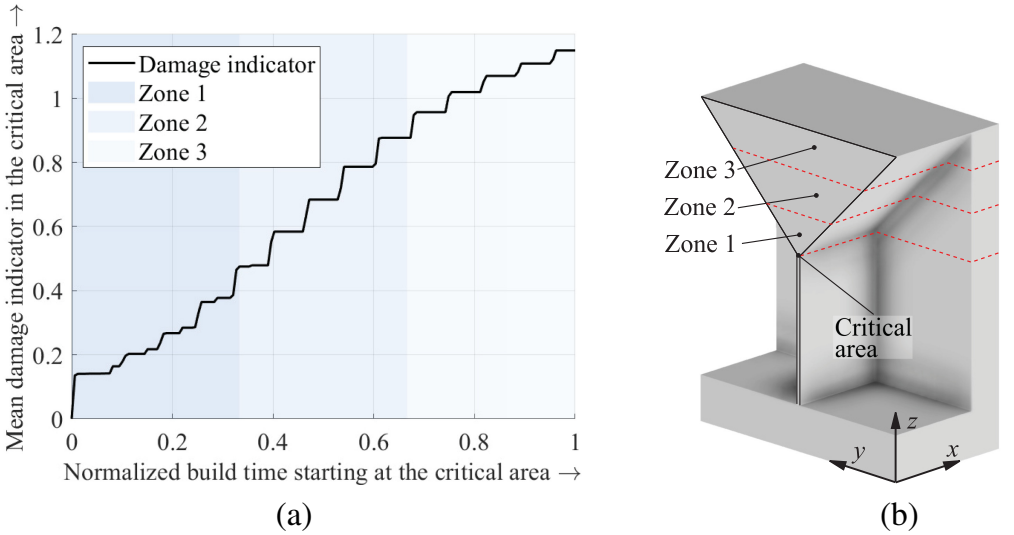

Fig. 6 Overview of the damage accumulation characteristics; (a) damage accumulation according to the implemented damage indicator; (b) allocation of the zones to the test specimen with *z* denoting the building direction.

- Zone 1: The first zone can be identified for the first third of the normalized building time. It is characterized by generally small damage indicator increases due to a small amount of bulk material, which cannot lead to a significant stress build-up. Also, the influence on the damage indicator increase of both the individual layer expansions as well as the warpage and deflection of the part can be seen by the repeating small step jumps in a comparatively short period of time. The high increase in the damage indicator after the first step is due to the expansion of the newly applied layer.
- Zone 2: This zone comprises the second third of the build time. Strong damage indicator increases can be identified, which is due to more material added during the manufacturing process leading to a stronger warpage of the prismatic volume. Only the influence of the part deflection can be seen because the effect of an expansion of the individual layers is compensated by the material below.
- Zone 3: The last region within the normalized build time is characterized by a continuously decreasing damage indicator rise. This is because of an overcompensation of the material stiffness growth compared with the stress build-up. Like in zone 2, no influence of the individual layers on the damage indicator can be seen.

The observation of this type of damage accumulation is also in accordance with measurements from Kruth et al.[23] Through these simulative investigations in this study, the functioning of the continuous summation of the damage indicator was verified, and physical interpretability of the results was ensured.

3.2 Validation

In the following, the conformity of the simulation results with the experimental findings depending on the chosen failure model and calibration approach is evaluated and discussed. For this, both a global and a local analysis were conducted.

3.2.1 *Pre-analyses*

In the sense of a pre-selection of appropriate failure models and their corresponding calibration approaches, the following analyses were conducted.

RT model. As stated in Panzer et al.,[14] the RT model predicted small values for the equivalent plastic failure strain $\varepsilon^{f}_{eq,RT}$ at high triaxialities. An immediately high-damage indicator with values significantly above 1.00 without a build-up of damage in these areas was to be expected.

This behavior could be seen during the simulative PBF-LB/M process over the course of this study (not shown). This led to extensive element deactivations, which did not correspond with the critical location suggested in Fig. 4. The representation of an actual damage accumulation, leading to residual stress-induced macroscopic cracking, was not realizable. Due to these observations, it can be concluded at this point that the RT model is not suitable for a PBF-LB/M fracture simulation. This is why it will not be considered further in the following, and the focus will be set on the JC model.

JC model. Over the course of the solely experimentally calibrated JC model, the influence of the temperature on the fracture behavior was considered, as described in Sec. 2.3.2. To investigate the impact of this parameter on the cracking susceptibility, specimen A and specimen B were simulated with the factor turned on and off, respectively.

In Fig. 7, the maximum damage indicators for specimen A and specimen B with the influence of the temperature parameter are visualized. For both samples, the damage indicator without the temperature factor is increased by approximately 65% compared with the damage indicator taking the thermal parameter into account. This is a valid result as the calibration results in Panzer et al.[14] showed an increasing equivalent plastic failure strain $\varepsilon^{f}_{eq,JC}$ with an increased temperature, by which a reduced cracking susceptibility could be expected.

However, to allow for comparability between the experimental calibration method and the remaining approaches, in which no thermal calibration was conducted, the temperature factor was turned off for the remaining validation simulations.

3.2.2 *Global analysis*

The simulative results for the various calibration approaches, along with an exemplary experimental result of specimen A and specimen B, are visualized in Figs. 8 and 9, respectively. The maximum values of the damage indicator were only reached in narrow regions. It becomes clear that the locations of an increased cracking susceptibility agree qualitatively for all three calibration approaches. In each case, the damage indicator reaches a higher value in the expected critical area (region 1), in the region between the cuboid of the sample and the build plate (region 2), and in the zone between the cuboid and the remaining specimen (region 3). For the latter, the speckled pattern with a spacing of approximately 1 mm along the build height is a result of the repeated layer compound activation process. It is also noticeable that, for region 1, the AM-adapted approach exhibited the most homogeneous and evenly distributed damage indicator, whereas the remaining approaches were characterized by a partly spotted raster in the mentioned region.

Where applicable, the regions of deactivated elements are framed by a dashed ellipse. Elements with damage indicator values higher than 1.00 persisting, despite an element deactivation, as described for each specimen in the following, can be reasoned by the fact that the element removal only takes place in the computational step after $D > 1.00$ was detected.

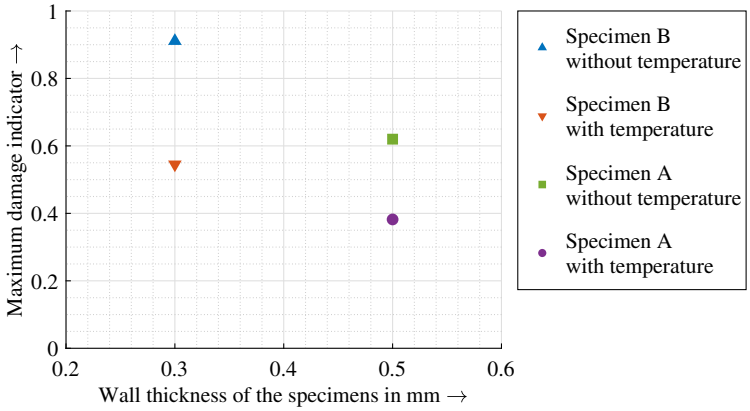

Fig. 7 Comparison of the influence of the temperature parameter in the experimental calibration on the damage indicator.

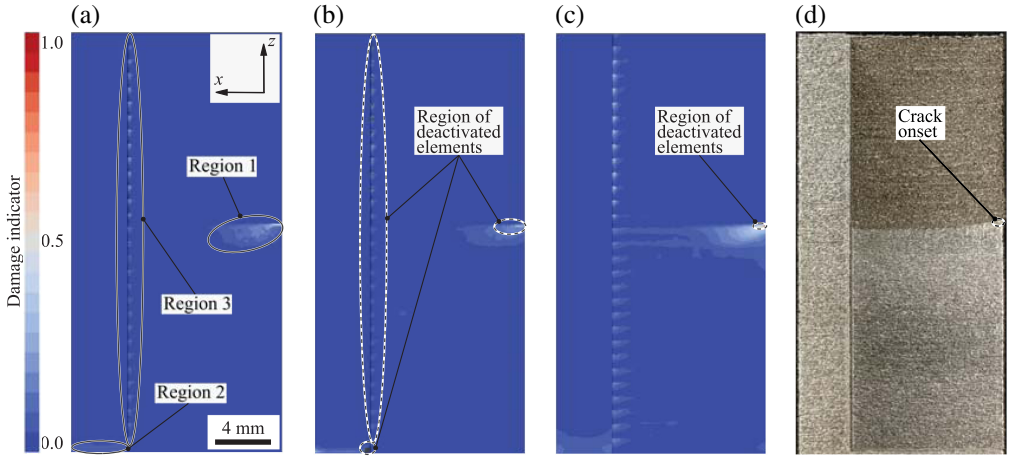

Fig. 8 Simulative and experimental results of the global analysis for specimen A with deactivated elements in the simulation and the crack in the manufactured specimen highlighted by dashed ellipses; *z* denotes the building direction; (a) simulation result for the experimental calibration approach; (b) simulation result for the experimental and simulative calibration approach; (c) simulation result for the AM-adapted calibration approach; (d) experimental result.

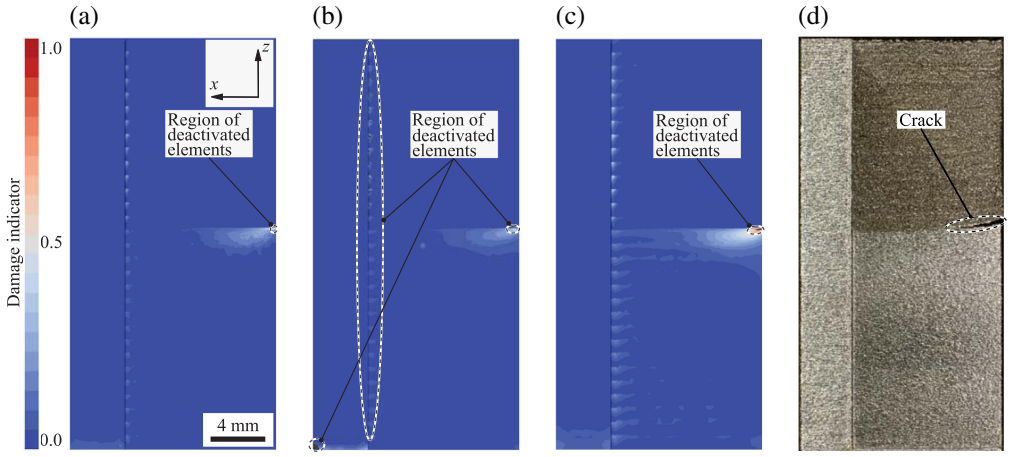

Fig. 9 Simulative and experimental results of the global analysis for specimen B; deactivated elements in the simulation and the crack in the printed specimen are highlighted by dashed ellipses; *z* denotes the building direction; (a) simulation result for the experimental calibration approach; (b) simulation result for the experimental and simulative calibration approach; (c) simulation result for the AM-adapted calibration approach; (d) experimental result.

Furthermore, as the graphical user interface (GUI) shows the fracture values in the nodes, some values for the damage indicator in the GUI might differ from the actual values in the integration points due to the extrapolation process of the integration point values to the nodes.

Results for specimen A. The highest value of the damage indicator for the purely experimental approach [see Fig. 8(a)] was reached in region 1 and accumulated to 0.62. The damage indicator values in the remaining zones did not exceed 0.30. Therefore, based on these findings, no crack initiation would have been predicted, and no element deactivation took place.

For the combined experimental and simulative calibration approach [see Fig. 8(b)], the damage indicator exceeded a value of 1000 in region 2, leading to a local element deactivation. Also, scattered elements in region 1 and region 3 were deactivated due to damage indicator values exceeding 1.00. Therefore, multiple onsets of cracks in all three regions were predicted by this approach.

The AM-adapted approach predicted the highest value for the damage indicator in region 1, where it reached 1.03 with a subsequent local element removal [see Fig. 8(c)]. In the remaining

regions, the damage indicator values did not exceed 0.50. Therefore, a slight fracture formation in the critical region was determined.

Analyzing a manufactured specimen of type A [see Fig. 8(d)] showed that only in region 1 a crack initiation did occur. In the other regions, no fracture formations could be observed. This leads to the conclusion that for the presented sample, the AM-adapted approach was the only one to appropriately represent the cracking behavior induced by residual stresses built up during PBF-LB/M.

Results for specimen B. The solely experimental calibration method predicted a maximum value of the damage indicator of 1.03 in region 1, by which a low number of elements was removed [see Fig. 9(a)]. Through this, a crack onset, but no indication of crack growth, was detected. The remaining regions did not exceed 0.30 and were, therefore, not determined as being susceptible to crack initiation.

For the experimental and simulative calibration method, a similar behavior as described for specimen A was observed for specimen B. In each of the three regions, a crack formation was predicted [see Fig. 9(b)]. The maximum damage indicator value was again determined in region 2 and accumulated to approximately 218.

The AM-adapted approach exhibited a maximum value of the damage indicator of 1.42 with a significant number of element deactivations in region 1 [see Fig. 9(c)]. Through this, both a crack onset and a subsequent crack propagation were predicted. The remaining areas with an increased damage indicator value did not exceed 0.50.

Through a comparison of the simulation results with an actually printed sample [see Fig. 9(d)], it became evident that, as for the previous specimen, the AM-adapted approach approximated the real cracking behavior in the best way. The experimental result showed a long crack in region 1, whereas no crack defects were observed in the remaining regions.

Discussion. The abovementioned observations of the AM-adapted approach predicting the real cracking behavior most adequately can be explained by evaluating the fitted calibration curves of the JC model in the strain-triaxiality space from Panzer et al.,[14] as visualized in Fig. 10.

The fitting curve of the experimental calibration approach predicts higher values for the equivalent plastic failure strain $\varepsilon_{\mathrm{eq}}^{\mathrm{f}}$, except for the triaxiality range between 0.38 and 0.78. Given the fact that most of the triaxiality values within the part were outside this segment, the cracking susceptibility predicted by this approach decreased.

The significantly increased number of elements deactivated when applying the combined experimental and simulative approach was due to the convergence of the graph toward zero at high triaxialities, leading to a strong reduction of bearable stresses and strains, resulting in premature fracturing.

Lastly, the fitting curve of the AM-adapted approach is characterized by a continuously lower equivalent plastic failure strain $\varepsilon_{\mathrm{eq}}^{\mathrm{f}}$ with a constant failure strain offset of 0.08 up to a

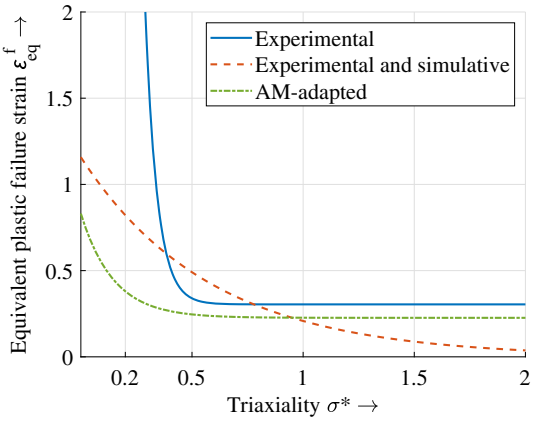

Fig. 10 Comparison of the fitting curves of the three calibration approaches for the JC model.[14]

triaxiality of 0.55 compared with the experimental approach. By this, the prediction of an earlier fracture formation can be explained.

Generally, it is recognizable that the AM-adapted fitting curve maintains a constant value over a wide range and is characterized by a slower increase of the failure strain with a decreasing triaxiality, compared with the experimental approach. This makes the AM-adapted approach more stable in terms of resulting failure strains at slight changes in the triaxiality. This explains the observation of a more homogeneously distributed damage indicator field with no partly spotted raster in region 1, as is the case for the alternative approaches.

3.2.3 *Local analysis*

The experimental and the combined experimental and simulative approaches are not further considered for the more detailed local analysis of region 1 as these approaches have already shown in the global analysis that they are not capable of predicting the cracking susceptibility with sufficient accuracy. Therefore, the following results apply only to the AM-adapted calibration approach.

Crack formation and propagation. A quantitative evaluation of the predicted and actual crack lengths for specimen A and specimen B is visualized in Fig. 11. As shown, the onset of a crack for specimen A was predicted well. The predicted crack length for specimen B, however, deviated from the actual fracture length by a factor of approximately 8, considering the mean fracture value.

This relationship was also recognized by Fischer et al.[20] for conventionally manufactured ductile materials. As the damage indicator has no influence on the elastic-plastic fracture analysis, by which a non-disturbed structure is investigated in the stress analysis, the damage indicator should only be used for the prediction of crack onsets. The crack propagation and crack path analysis with the damage indicator should be seen skeptically. A similar statement was placed by Hancock and Mackenzie.[24] They concluded that the approach using the damage indicator is appropriate to capture a failure initiation in multi-axial stress fields. In the case of non-uniform stress fields, as they occur ahead of cracks, this statement might not be supportable anymore.

It was also recognized that the local scan strategy at the crack-susceptible location has a strong influence on the resulting crack lengths.[7] This was attributed to varying energy input and, as a result, to the formation of varying defects and microstructures. The same applies to the laser beam profile, which also changes the local energy input and, therefore, can be assumed to affect the crack length. As neither the scan strategy nor the laser beam profile was considered in the utilized macroscopic PBF-LB/M process simulation, such effects cannot be taken into account. This may be another reason for the observed deviations between the simulations and the experiments.

Figure 12 demonstrates the predictive capabilities concerning the crack path and the crack propagation direction of the simulation for specimen B. The crack propagated mostly in the

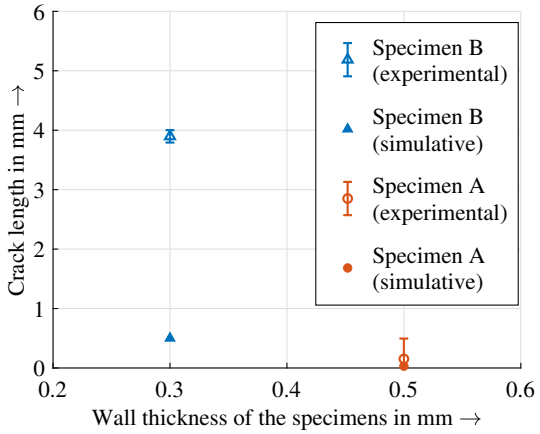

Fig. 11 Comparison of the simulatively predicted and experimental crack lengths.

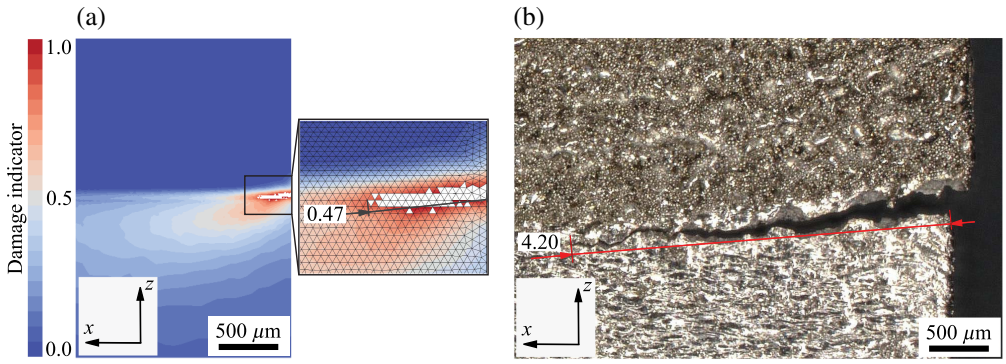

Fig. 12 Comparison of the crack path and the crack propagation direction for the simulation and the experiment of specimen B with z denoting the building direction and dimensions in mm: (a) simulative result and (b) experimental result.

direction of the x-axis. Furthermore, a straight crack without a recognizable zigzag pattern,[25] even though this is typical for ductile materials,[26,27] can be seen in Fig. 12(a).

Both characteristics were in accordance with the experimental results, visualized in Fig. 12(b). The presence of a non-zigzag crack can be reasoned by the fact that the top prism part of the sample had a significantly higher thickness than the bottom wall, making a crack deflection in this direction energetically inefficient.

Crack appearance. Extracting the deactivated elements from the simulation of specimen B resulted in the visualization of the actual crack [see Fig. 13(a)]. The starting point of the crack is shaped like an arc, turned upward (highlighted by the dashed white line). With increasing crack growth, this bending direction reverses (marked by the continuous black line). The outside part of the crack on the sides of the wall remains unchanged, resulting in the previously described mostly horizontal crack propagation.

These descriptions also match with the experimental results, as shown in Fig. 13(b), where a multi-focus in the x-direction was applied. The upturned arc crack surface at the front with the subsequent reversal (both highlighted in accordance with the simulation result) are clearly distinguishable.

The upturned fracture surface can be explained by the circumstance that the fracture did not have its starting point at the very front of the specimen but on its wall side close to the front of the sample, as a retracing by the numerical simulations showed. Taking into consideration that the plane of the maximum plastic strain is orientated by an angle of 45 deg to the actual crack plane in a plane strain mode I loading,[25,28] this initial crack propagation direction in the positive and negative direction of the y-axis, respectively, can be explained. The subsequent crack propagation toward the x-axis direction exhibits shear lips at a 45 deg angle in the y–z-plane, as also observed by Anderson[25] for crack formations in conventionally fabricated materials.

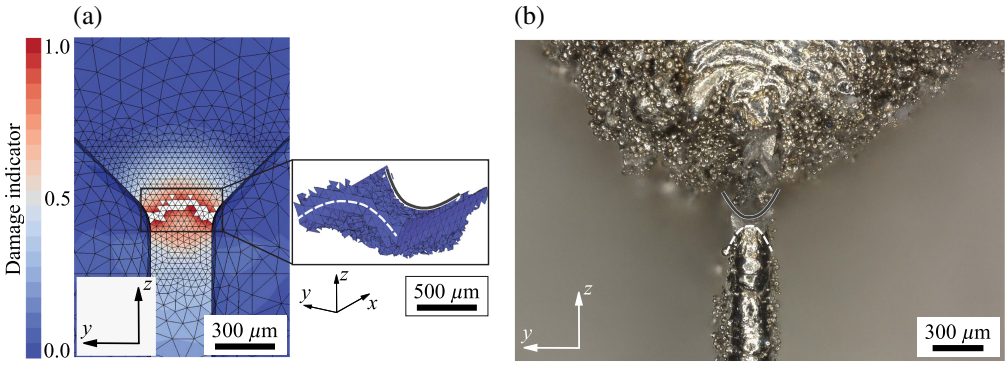

Fig. 13 Comparison of the crack appearance for the simulation and the experiment of specimen B with z denoting the building direction; (a) simulative result and (b) experimental result.

3.3 Performance Analysis

For further investigation of the performance of the implementations in computational effort and predictive capabilities compared with results from the literature, the following analyses were performed and evaluated.

3.3.1 *Computation time analysis*

The additional computational effort required by the fracture implementations was evaluated by comparing the real simulation time of the standard PBF-LB/M process simulation with that of the fracture simulation for specimen A. Each simulation was performed on a workstation utilizing 32 logical central processing unit cores of the type Intel® Xeon® Gold 6248 at a frequency of 2.50 GHz and with 728 GB random-access memory.

The computing time for the standard PBF-LB/M simulation of specimen A took approximately 388 min, whereas the time for the extended simulation approach was 391 min. Therefore, an increase in the computational effort of 0.65% was identified. This can be seen as small, which highlights the time efficiency of the proposed method for detecting cracking susceptible regions in PBF-LB/M parts.

3.3.2 *Material parameters from the literature*

Ressa[19] calibrated the JC model for conventionally manufactured IN718, with the calibration constants shown in Table 2. As shown in Panzer et al.,[14] the fitting curve using the results from Ressa[19] tended toward smaller values of the equivalent plastic failure strain $\varepsilon_{\mathrm{eq}}^{\mathrm{f}}$ at high triaxialities, compared with the calibrations with PBF-LB/M-manufactured parts. This led to a similar behavior during the simulation of the manufacturing and crack formation process as it was explained for the RT model at the beginning of Sec. 3.2.1.

Through this, it can be concluded that using material parameters of conventional IN718 for the JC failure model, as they were obtained by Ressa,[19] is not suitable to predict the macroscopic crack formation during the PBF-LB/M manufacturing process.

4 Conclusion and Outlook

Over the course of this study, the RT and the JC failure models, each calibrated by three different approaches, were evaluated concerning their predictive capabilities with respect to fracture initiation and propagation due to residual stresses during the PBF-LB/M process in IN718 parts. Through this, the underlying formulas and the operating principle of the fracture implementations were described. After verification of the extended code structure, a validation regarding the global and local predictability of cracks was performed. Last, the efficiency of the crack-determining approaches was quantified, and the usability of calibration values of conventional material was analyzed.

The main conclusions of the conducted investigations are outlined below:

- In general, the ductile damage initiation criteria proved to be an appropriate means to model failure within PBF-LB/M parts made from IN718. The presented approaches are capable of capturing the failure accumulation during the manufacturing process due to a build-up of residual stresses and plastic strains. Both the global as well as the local fracture behavior were adequately predicted.

  The computation time of the simulations including the fracture extensions compared with the standard thermo-mechanical simulations only increased by 0.65%. This emphasizes the efficiency of the failure model approaches in FE computations.
- The JC model calibrated by the AM-adapted approach allowed for a reliable prediction of fracture formation in the PBF-LB/M-manufactured parts. None of the calibrated RT models provided physically sensible values in terms of the proposed damage indicator. The calibration results of conventionally manufactured IN718 parts were not useful for the prediction of cracking in additively manufactured parts.
- The implemented models were not able to represent the actual crack lengths in the validation geometries. However, the industrial relevance of the prediction of crack onsets is to

be emphasized. The crack path and the crack propagation direction were captured correctly. The general crack appearance was also represented accurately.

Based on these findings, the implementations can be utilized to increase the process understanding regarding crack initiation and formation. Also, the models can be used to determine at which point during the building process a crack formation occurs and, therefore, allow for an *a priori* adaption of the geometry accordingly. The proposed methodology may be also applicable to crack predictions between the solid part and the support structure.

Besides the linear damage indicator approach, non-linear damage accumulation functions also exist in the literature, as for example proposed by Bai.[29] These could further increase the predictive capabilities for a crack formation, under the consideration that a damage accumulation even under proportional loading is not linear. Besides the two utilized failure-defining parameters σ^* and $\varepsilon_{\mathrm{eq}}^{\mathrm{f}}$, the Lode angle as a third parameter could also be used for the enhancement of fracture predictions.[30]

The quantification of cracking probabilities due to statistical effects during the PBF-LB/M process and dependent on influencing factors, such as the part position on the build platform or the local hatching strategy, should be named as an additional scope for future work. For this purpose, additional samples with an increased quantity need to be manufactured for a reliable database.

Lastly, predicting the change of the cracking susceptibility as a function of the process parameters, which may be locally modified, and the resulting microstructure is another goal for future studies to further enhance the PBF-LB/M process.

5 Appendix A: Model Calibration Constants

In Table 2, the calibration constants for the utilized failure models are listed. These values were determined by Panzer et al.[14] and Ressa,[19] applying different calibration approaches.

Table 2 Calibration constants for the utilized models and calibration approaches based on Panzer et al.[14] and Ressa.[19]

	Experimental approach[14]	Experimental and simulative approach[14]	AM-adapted approach[14]	Conventional[19]
RT	$\varepsilon_0^{\mathrm{RT}} = 0.5134$	$\varepsilon_0^{\mathrm{RT}} = 0.6116$	$\varepsilon_0^{\mathrm{RT}} = 0.3307$	N/A
JC	$d_1 = 0.3042$	—	—	—
	$d_2 = 362.072$	$d_1 = 0.0$	$d_1 = 0.226$	$d_1 = 0.0988$
	$d_3 = -18.485$	$d_2 = 1.158$	$d_2 = 0.604$	$d_2 = 0.4493$
	$d_4 = 0.0465$	$d_3 = -1.717$	$d_3 = -6.844$	$d_3 = -1.1492$
	$d_5 = 4.2307$	—	—	—

Disclosures

The authors declare no conflict of interest.

Code and Data Availability

The raw data and the processed data required to reproduce the findings presented in this paper can be made available upon request.

Author Contributions

Hannes Panzer: conceptualization (lead), formal analysis (lead), investigation (lead), methodology (lead), software (lead), validation (lead), visualization (lead), writing—original draft (lead). Daniel

Wolf: conceptualization (supporting). Michael F. Zaeh: funding acquisition (supporting), project administration (supporting), resources (supporting), supervision (supporting), writing—review and editing (supporting).

Acknowledgments

We would like to thank Mr. Ulrich Fleck from the Oerlikon AM Europe GmbH for his support in separating the validation geometries from the build plate using electrical discharge machining.

References

1. E. M. Sefene, "State-of-the-art of selective laser melting process: a comprehensive review," *J. Manuf. Syst.* **64**, 250–274 (2022).
2. D. D. Singh, T. Mahender, and A. R. Reddy, "Powder bed fusion process: a brief review," *Mater. Today:. Proc.* **46**, 350–355 (2021).
3. B. Gao et al., "A review of research progress in selective laser melting (SLM)," *Micromachines* **14**(1), 57 (2022).
4. H. Jia et al., "Scanning strategy in selective laser melting (SLM): a review," *Int. J. Adv. Manuf. Technol.* **113**(9–10), 2413–2435 (2021).
5. J. L. Bartlett and X. Li, "An overview of residual stresses in metal powder bed fusion," *Addit. Manuf.* **27**, 131–149 (2019).
6. J. Platl et al., "Cracking mechanism in a laser powder bed fused cold-work tool steel: the role of residual stresses, microstructure and local elemental concentrations," *Acta Mater.* **225**, 117570 (2022).
7. H. Panzer et al., "Experimental investigation of process parameter variations on the microstructure and failure behavior of IN718 structures in PBF-LB/M," *J. Laser Appl.* **36**(1), 012015 (2024).
8. D. Lyu et al., "Numerical prediction of residual deformation and failure for powder bed fusion additive manufacturing of metal parts," *J. Mech.* **36**(5), 623–636 (2020).
9. Y. Zhang and J. Zhang, "Finite element simulation and experimental validation of distortion and cracking failure phenomena in direct metal laser sintering fabricated component," *Addit. Manuf.* **16**, 49–57 (2017).
10. H. T. Tran et al., "A new method for predicting cracking at the interface between solid and lattice support during laser powder bed fusion additive manufacturing," *Addit. Manuf.* **32**, 101050 (2020).
11. H. T. Tran, X. Liang, and A. C. To, "Efficient prediction of cracking at solid-lattice support interface during laser powder bed fusion via global-local J-integral analysis based on modified inherent strain method and lattice support homogenization," *Addit. Manuf.* **36**, 101590 (2020).
12. H. T. Tran and A. C. To, "Cracking prediction at solid-tooth support interface during laser powder bed fusion additive manufacturing," *J. Sci.: Adv. Mater. Devices* **8**(4), 100615 (2023).
13. Y. Bresson et al., "Numerical modelling of parts distortion and beam supports breakage during selective laser melting (SLM) additive manufacturing," *Int. J. Adv. Manuf. Technol.* **119**, 5727–5742 (2022).
14. H. Panzer et al., "Towards a simulation-assisted prediction of residual stress-induced failure during powder bed fusion of metals using a laser beam: suitable fracture mechanics models and calibration methods," *J. Manuf. Mater. Process.* **7**(6), 208 (2023).
15. J. R. Rice and D. M. Tracey, "On the ductile enlargement of voids in triaxial stress fields," *J. Mech. Phys. Solids* **17**(3), 201–217 (1969).
16. G. R. Johnson and W. H. Cook, "Fracture characteristics of three metals subjected to various strains, strain rates, temperatures and pressures," *Eng. Fract. Mech.* **21**(1), 31–48 (1985).
17. F. A. Bayerlein, "Managing form deviation in laser beam melting by pre-deformation," PhD thesis, Technical University of Munich (2020).
18. G. Dhondt, "CalculiX CrunchiX User's Manual Version 2.20," http://www.dhondt.de/ccx_2.20.pdf (2022).
19. A. Ressa, "Plastic deformation and ductile fracture behavior of Inconel 718," Master's thesis, The Ohio State University (2015).
20. F. D. Fischer et al., "A note on calibration of ductile failure damage indicators," *Int. J. Fract.* **73**(4), 345–357 (1995).
21. M. Gao and R. Krishnamurthy, "Critical strain based ductile damage criterion and its application to mechanical damage in pipelines," in *13th Int. Conf. Fract.* (2013).
22. Special Metals Corporation, "Inconel alloy 718," Data sheet SMC-045 (2007).
23. J.-P. Kruth et al., "Assessing and comparing influencing factors of residual stresses in selective laser melting using a novel analysis method," *Proc. Inst. Mech. Eng., Part B: J. Eng. Manuf.* **226**(6), 980–991 (2012).
24. J. Hancock and A. Mackenzie, "On the mechanisms of ductile failure in high-strength steels subjected to multi-axial stress-states," *J. Mech. Phys. Solids* **24**(2–3), 147–160 (1976).
25. T. L. Anderson, *Fracture Mechanics: Fundamentals and Applications*, CRC Press (2017).
26. C. D. Beachem and G. R. Yoder, "Elastic-plastic fracture by homogeneous microvoid coalescence tearing along alternating shear planes," *Metallurg. Trans.* **4**(4), 1145–1153 (1973).

27. J. P. Gudas, *Micromechanisms of Fracture and Crack Arrest in Two High Strength Steels*, University Microfilms International Dissertation Services (1986).
28. W. Becker and S. Lampman, *Fracture Appearance and Mechanisms of Deformation and Fracture*, ASM International (2002).
29. Y. Bai, "Effect of loading history on necking and fracture," PhD Thesis, Massachusetts Institute of Technology (2007).
30. Y. Bai and T. Wierzbicki, "A new model of metal plasticity and fracture with pressure and Lode dependence," *Int. J. Plast.* **24**(6), 1071–1096 (2008).

Hannes Panzer received his BSc degree in mechanical engineering from TUM, awarded in 2018, and his MSc degree in automotive engineering, also from TUM, awarded in 2021. His master's thesis focused on creating a simulation model to characterize crack formation in structural components during PBF-LB/M. He has been pursuing a doctoral degree in additive manufacturing at TUM, with a focus on simulating PBF-LB/M to study microstructure evolution and crack formation since 2021.

Biographies of the other authors are not available.